Draft version April 5, 2019
Typeset using LaTeX **twocolumn** style in AASTeX62

Constraining Mass Transfer Histories of Blue Straggler Stars with COS Spectroscopy of White Dwarf Companions

Natalie M. Gosnell,[1] Emily M. Leiner,[2,3] Robert D. Mathieu,[2] Aaron M. Geller,[3,4] Christian Knigge,[5] Alison Sills,[6] Nathan W. C. Leigh,[7,8] and Phillip Cargile[9]

[1]*Department of Physics, Colorado College, 14 E. Cache La Poudre St, Colorado Springs, CO 80903, USA*
[2]*Department of Astronomy, University of Wisconsin - Madison, 475 N. Charter Street, Madison, WI 53706, USA*
[3]*Center for Interdisciplinary Exploration and Research in Astrophysics (CIERA) and Department of Physics and Astronomy, Northwestern University, 2145 Sheridan Rd, Evanston, IL 60208, USA*
[4]*Adler Planetarium, Department of Astronomy, 1300 S. Lake Shore Drive, Chicago, IL 60605, USA*
[5]*School of Physics and Astronomy, University of Southampton, Highfield, Southampton, SO17 IBJ, UK*
[6]*Department of Physics and Astronomy, McMaster University, 1280 Main St. W, Hamilton, ON L8S 4M1, Canada*
[7]*Departamento de Astronomía, Facultad de Ciencias Físicas y Matemáticas, Universidad de Concepción, Concepción, Chile*
[8]*Department of Astrophysics, American Museum of Natural History, Central Park West and 79th Street, New York, NY 10024, USA*
[9]*Department of Astronomy, Harvard University, Cambridge, MA, 02138, USA*

ABSTRACT

Recent studies show that the majority of blue straggler stars in old open clusters are formed through mass transfer from an evolved star onto a main sequence companion, resulting in a blue straggler and white dwarf in a binary system. We present constraints on the formation histories and mass transfer efficiencies for two blue straggler-white dwarf binaries in open cluster NGC 188 resulting from measuring white dwarf cooling temperatures and surface gravities with *HST* COS far-ultraviolet spectroscopy. We determine that one system, WOCS 4540, formed through Case C mass transfer resulting in a CO-core white dwarf with a temperature of 17200^{+100}_{-80} K and a $\log g$ of $7.76^{+0.03}_{-0.01}$. These fitted values correspond to a mass of $0.50^{+0.05}_{-0.01}$ $M_{\odot}$ and an age of 94^{+7}_{-3} Myr. The other system, WOCS 5379, formed through Case B mass transfer resulting in a He-core white dwarf with a temperature of 15400^{+280}_{-260} K and a $\log g$ of $7.45^{+0.06}_{-0.06}$, corresponding to a mass of $0.40^{+0.04}_{-0.04}$ $M_{\odot}$ and an age of 230^{+22}_{-23} Myr. We determine possible progenitor binary systems with a grid of accretion models using MESA, and investigate whether these systems would lead to stable or unstable mass transfer. WOCS 4540 likely resulted from stable mass transfer during periastron passage in an eccentric binary system, while WOCS 5379 challenges our current understanding of the expected regimes for stable mass transfer from red giant branch stars. Both systems are examples of the benefit of using a detailed analysis to fine-tune our physical understanding of binary evolutionary processes.

Keywords: binaries: close, blue stragglers, open clusters and associations: individual (NGC 188), stars: evolution, white dwarfs

1. INTRODUCTION

Thorough studies of old open clusters reveal a variety of stellar populations that do not follow single-star evolutionary pathways (e.g., Landsman et al. 1997; Geller et al. 2017; Mathieu & Leiner 2019). Stars that fall in unexpected areas of an optical color-magnitude diagram (CMD) or Hertzsprung-Russell (HR) Diagram have histories that have altered the stellar temperature, luminosity, or both. In evolved open clusters, these alternative pathway stellar products can make up to 25% of the total evolved stellar population (Mathieu & Geller 2015; Gosnell et al. 2015). In open clusters, the majority of these stars are categorized as blue straggler stars (BSSs).

BSSs are traditionally empirically defined to be stars bluer and brighter than the main sequence turnoff (Sandage 1953). They are found in many stellar populations, including in globular clusters (e.g., Piotto et al. 2004; Knigge et al. 2008) and in the field as blue metal-poor stars (Preston & Sneden 2000; Carney et al. 2001). In order to appear in this region of a CMD, enough mass must be added to a main sequence star such

ngosnell@coloradocollege.edu

that it exceeds the current main sequence turnoff mass. In old open clusters, this process happens predominantly through binary mass transfer (Geller & Mathieu 2011; Gosnell et al. 2015). It is also possible to create a BSS through a Kozai-driven merger in a triple system (Perets & Fabrycky 2009; Naoz & Fabrycky 2014), and through collisions in more dynamically-active environments such as globular cluster cores (e.g., Leigh et al. 2011).

Across multiple open clusters and in the field, BSSs are predominantly found in wide binaries with periods of approximately 1000 days, some of which are circularized, which is in contrast to main sequence binaries at the same periods that are almost all eccentric (Carney et al. 2001; Sneden et al. 2003; Latham 2007; Geller et al. 2009). These orbital periods are consistent with the final orbital periods expected after mass transfer from an asymptotic giant branch (AGB) star onto a main sequence companion, known as Case C mass transfer (Chen & Han 2008; Gosnell et al. 2014). This process results in a BSS with the remnant core of the giant star donor as a companion, observed as a CO-core white dwarf (WD) (Paczyński 1971). BSSs can also form as a result of mass transfer from a red giant branch (RGB) star, known as Case B mass transfer, which results in a BSS with a He-core WD companion at a shorter binary period of approximately 100 days (Chen & Han 2008).

The *Gaia* mission (Gaia Collaboration et al. 2016) continues to improve our understanding of cluster populations (e.g., Choi et al. 2018) and discover new open clusters that were previously unknown (e.g., Cantat-Gaudin et al. 2018). As a result, many more alternative pathway stellar evolutionary products will be uncovered. Placing these products in context within stellar evolutionary processes at large requires knowing the formation mechanisms responsible for and the future evolution of these systems. In this paper we focus on the BSS population of NGC 188 in order to constrain the possible mass transfer histories that are responsible for creating the majority of open cluster BSSs (Gosnell et al. 2015).

1.1. *The NGC 188 Blue Straggler Population*

The old open cluster NGC 188 has one of the most thoroughly studied BSS populations to date. The cluster contains 21 confirmed BSSs, the majority of which are in long-period binary systems with known periods and eccentricities (Mathieu & Geller 2009, and references therein). An additional UV-bright BSS in NGC 188 was detected in Subramaniam et al. (2016), but it does not have confirmed kinematic membership. Gosnell et al. (2014) and Gosnell et al. (2015) detected WD companions of 7 kinematic member BSSs using far-ultraviolet photometry, as shown in Figure 1. The presence of a WD in binaries with periods appropriate for Case B or Case C mass transfer indicates that these BSS-WD systems are post-mass transfer binaries. Taking into account WD detection limits, Gosnell et al. (2015) estimate that 67% of the NGC 188 BSSs form through mass transfer.

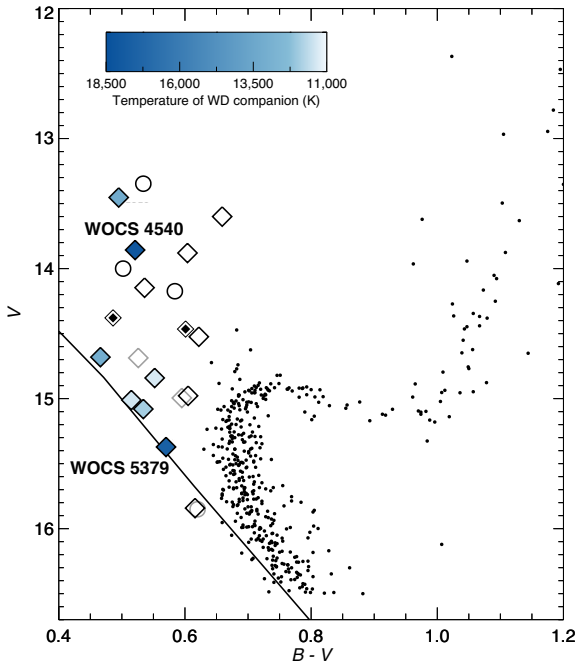

Figure 1. From Gosnell et al. (2015), a CMD of NGC 188 cluster members. The solid black line shows the zero-age main sequence. The BSS symbols indicate binarity (diamonds: binary, double diamond: double-lined binary, circle: non-velocity variable). BSS with photometric WD detections are filled in with a color from light to dark blue, indicating the approximate temperature of the WD companion. Hotter WD companions are younger. The two BSS in this study, WOCS 4540 and WOCS 5379, are labeled.

The presence of a moderate temperature WD companion in a post-mass transfer system sets the timeline of the mass transfer history. The WD cooling age is a measure of the time since mass transfer ended (Gosnell et al. 2014). This timeline, combined with the age and current main sequence turnoff mass of the cluster, provides important constraints on the progenitor (pre-mass transfer) system. Possible histories for the three most recently formed BSSs in NGC 188 were presented in Gosnell et al. (2014), but the specifics of the mass transfer physics depend heavily on the giant star core mass, which becomes the WD mass. In order to better

constrain the pre- and post-mass transfer systems and to constrain the specific mass transfer histories responsible, in this paper we present *Hubble Space Telescope* Cosmic Origins Spectrograph (COS) spectra of WD companions of two BSS systems in NGC 188: WOCS 4540 and WOCS 5379. In Section 2 we outline the observations and in Section 3 we detail the spectral analysis that yields WD masses and cooling ages. These masses and ages inform the possible mass transfer histories explored in Section 4, and we provide our Summary in Section 5.

2. OBSERVATIONS

WOCS 5379 and WOCS 4540 were observed with COS on 2014 Nov 4 and 2014 Nov 10, respectively. Both targets were observed in TIME-TAG mode through the Primary Science Aperture (PSA) using the G140L grating with a central wavelength of 1105Å. This region covers the Lyman-α wings while also providing the wide wavelength coverage necessary to fit WD atmosphere models in this region alone. Each target was observed for 6 orbits. The data were reduced through the MAST pipeline. To increase the signal-to-noise per resolution element, we binned every 30 resolution elements in each spectrum resulting in a final wavelength resolution of 2.4Å.

In both sources, the contribution from the BSS is seen in the red end of the spectrum. In order to isolate the WD emission, we exclude flux redward of 1725Å for WOCS 5379 and 1600Å for WOCS 4540. The BSS in WOCS 4540 is brighter and hotter than WOCS 5379 (see Table 1, Gosnell et al. (2015)) so a larger contamination is expected. We also mask out by hand geocoronal emission lines and one ISM absorption feature evident in the spectrum. The spectra are de-reddened assuming $E(B-V) = 0.09$ (Sarajedini et al. 1999). The binned, de-reddened spectra are shown in Figures 2 and 3. The regions masked from any spectral fits are shown with grey shading.

3. ANALYSIS

3.1. *Spectral Fitting with* `emcee`

In order to determine the physical parameters of the WDs, the observed spectra are fit with model WD atmospheres using the python package `emcee`, an MCMC sampler (Foreman-Mackey et al. 2013). WD atmospheres are characterized by $T_{\rm eff}$ and $\log g$. Both observed spectra are fit using a grid of WD atmosphere models ranging from 11,000 K to 35,000 K in $T_{\rm eff}$ and from 6.0 to 9.0 in $\log g$ in steps of 0.25 (Koester 2010). The models assume a thick H-atmosphere with $M_H/M_{tot} = 10^{-4}$. Interpolation between the grid models is carried out with RegularGridInterpolator from `scipy` (Jones et al. 2001–).

The normalization of a WD model atmosphere to the observed spectrum is based on the ratio of the WD radius and the distance to the WD, r^2/d^2. Typically, when fitting a single spectral region this normalization results in fits that are degenerate in $T_{\rm eff}$ and $\log g$. The degeneracy can be broken, however, if the distance to the WD is known.

3.1.1. *Distance to NGC 188*

In order to determine a distance to NGC 188, we make use of *Gaia* DR2 (Gaia Collaboration et al. 2018b) astrometry to identify probable cluster members and infer a distance based on their measured parallaxes. We assemble a catalog for NGC 188 by selecting all stars in *Gaia* DR2 falling within a cone search based on the cluster center given in Kharchenko et al. (2013). We use a search radius of twice the apparent cluster radius to include as many NGC 188 stars as possible, resulting in a catalog of 45,519 *Gaia* DR2 sources.

We identify likely NGC 188 cluster members by running the HDBSCAN clustering algorithm (Campello et al. 2013) on the*Gaia* DR2 proper motions and parallaxes for stars in our cone search. HDBSCAN identifies clusters in datasets based on the density of points in high dimensional space and, importantly, does not force all data points to belong to a detected cluster. It also has the flexibility to allow the density of points in a cluster to vary. Advantages HDBSCAN has over other clustering algorithms are that there is only one important and relatively intuitive free parameter, the minimum cluster size of 30 stars, and it returns individual membership probabilities for every data point in a cluster.

Following Lindegren et al. (2018) and Gaia Collaboration et al. (2018a), we first filter out any source in our *Gaia* cone search catalog with failed astrometric solutions. From the most stable cluster HDBSCAN finds in the astrometric data, we select all stars with cluster membership probabilities greater than 90%, a relatively conservative cut on membership probability to insure few non-member contaminants when fitting for the cluster distance. Our final HDBSCAN based membership catalog contains 112 likely NGC 188 stars.

A full Bayesian inference is the recommended method for obtaining distances from observed *Gaia* parallaxes (Luri et al. 2018). This is particularly true given the nonlinearity between the astrophysical (distance) and measured (parallax) quantities, and the constraint that the former be necessarily positive while the latter is allowed to be zero or negative. We adopt a hierarchical Bayesian approach which assumes there is a parent

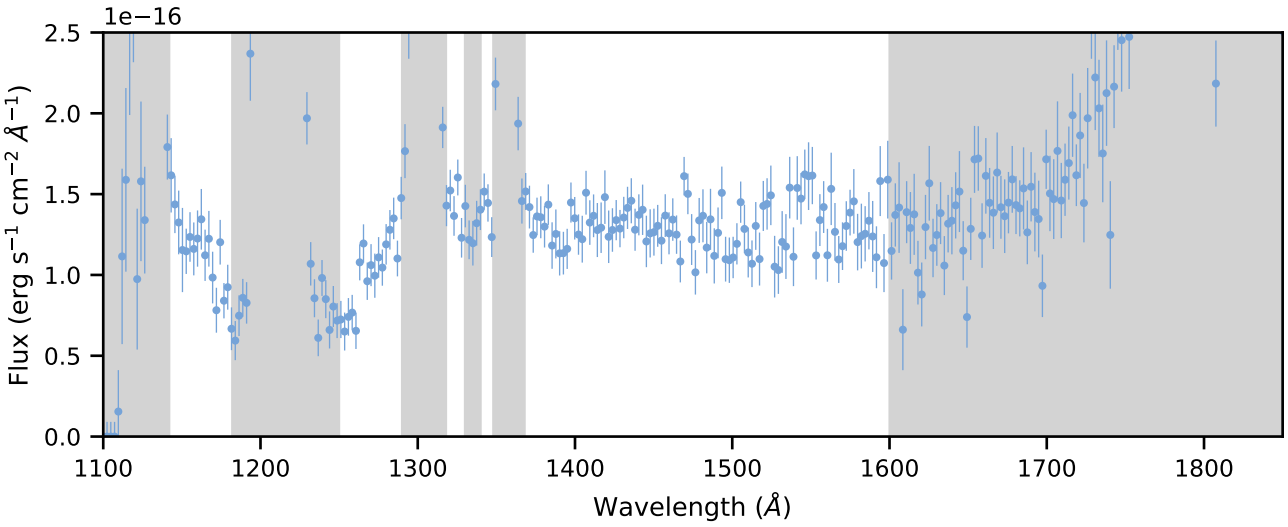

Figure 2. The de-reddened, binned *HST* COS spectrum of WOCS 4540, adopting $E(B-V) = 0.09$ (Sarajedini et al. 1999). The WD spectrum is contaminated with geocoronal emission lines, one ISM absorption feature, and emission from the BSS at longer wavelengths. The areas masked out in gray are excluded from later analysis and spectral modeling. WOCS 4540 is brighter than WOCS 5379, resulting in more contamination on the red end of the spectral region.

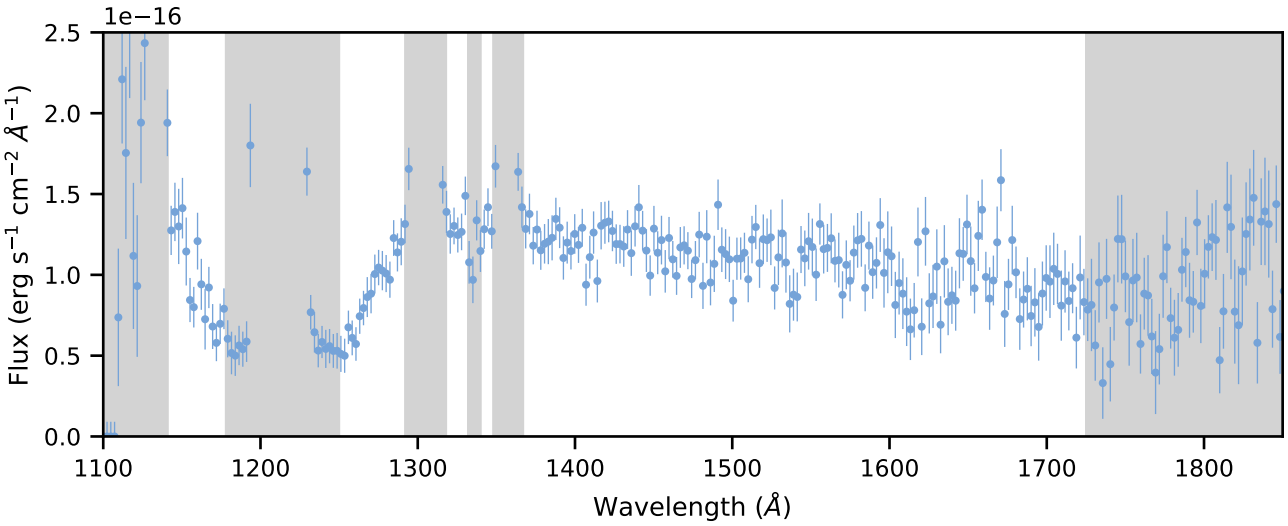

Figure 3. De-reddened, binned *HST* COS spectrum of WOCS 5379, with similar masking as in Figure 2.

model (a Plummer-density sphere) for the cluster with some dispersion. We infer the physical parameters of this distribution $(X, Y, Z, \sigma_X, \sigma_Y, \sigma_Z)$ by sampling the positional (RA/Dec) and parallax posterior distributions (assumed to be normal distributions with centroids and sigmas based on the *Gaia* DR2 measurements) for the individual stars in the cluster. We apply uninformative priors:

$$X = [-20, 0] \text{ kpc}$$

$$Y = [-20, 20] \text{ kpc}$$

$$Z = [0, 20] \text{ kpc}$$

$$\sigma_{X,Y,Z} = [0, 0.1] \text{ kpc}$$

We estimate the posterior distribution of the hierarchical cluster model with the nested sampler `dynesty`[1], using 250 live points, random walk sampling, and a stopping criteria if the change in evidence is $\Delta \log z = 0.01$. The resulting marginalized output parameters for NGC 188 based on this analysis are:

$$X = -9.236 \text{ kpc}, \ \sigma_X = 13 \text{ pc}$$

$$Y = 1.524 \text{ kpc}, \ \sigma_Y = 8 \text{ pc}$$

$$Z = 0.817 \text{ kpc}, \ \sigma_Z = 13 \text{ pc}$$

Projecting these galactocentric coordinates back into a heliocentric reference frame, the inferred distance to NGC 188 is 1955±11 pc.

Other assumptions about the cluster distance are possible, including previous photometric distances (1940 ± 70 pc, Sarajedini et al. 1999), distances calibrated with an eclipsing binary system (1770 ± 75 pc, Meibom et al. 2009), or adopting the individual *Gaia* DR2 parallax distances for WOCS 4540 (1980 ± 70 pc) and WOCS 5379 (1780 ± 90 pc, Bailer-Jones et al. 2018; Gaia Collaboration et al. 2018b). All of the these distances are consistent to each other within 2 sigma. The resulting WD parameters fit at each distance are very similar and the interpretation of the system formation histories given in Section 4 are the same. Since the final scientific results are consistent across these distances we adopt a single value of the *Gaia*-calculated cluster distance of 1955 pc for the rest of our analysis.

3.1.2. *Fitting Methodology*

We take advantage of these systems existing within a cluster by simultaneously fitting both spectra, assuming they are at the same distance. The Lyman-alpha region of a WD spectrum alone is not sufficient to constrain the distance to these objects, as a reasonable fit is possible at all $\log g$ values (Landsman et al. 1996). Therefore, the distance assumed for each simultaneous fit is selected randomly from a Plummer density distribution (Plummer 1911) at a distance of 1955 pc with a Plummer radius of 11 pc. After the distance is selected, the normalization factor is calculated by finding the corresponding WD radius for a given pair of $T_{\rm eff}$ and $\log g$ values, but the radius also depends on the core composition of the WD (Holberg & Bergeron 2006; Tremblay et al. 2011; Althaus et al. 2013).

Case B and Case C mass transfer processes result in different WD core compositions, with Case B systems resulting in He-core WDs and Case C systems resulting in CO-core WDs. Parsons et al. (2017) find that all CO-core WDs in their sample of eclipsing WD binaries have masses above 0.50 $M_\odot$, while all He-core WDs have masses below 0.50 $M_\odot$. Although it is possible to create CO-core WDs with masses below 0.50 $M_\odot$ (Han et al. 2000; Willems & Kolb 2004; Prada Moroni & Straniero 2009), the necessary scenarios require close binaries with a giant star mass of approximately 2.5 $M_\odot$. From previous photometric detection of the WDs in WOCS 4540 and WOCS 5379 (Gosnell et al. 2014, 2015), we know that these systems formed within the last 300 Myr when the turnoff mass of NGC 188 would only be 1.1–1.2 $M_\odot$. As this mass is well below the 2.5 $M_\odot$ required to form an under-massive CO-core WD, we assume that this scenario is not possible for these mass transfer systems in NGC 188, so we set a uniform $\log g$ prior for a CO-core WD between 7.74 and 9.0, corresponding to an approximate minimum WD mass of 0.50 $M_\odot$ for a moderate temperature WD (Tremblay et al. 2011). As He-core WDs are all expected to be below 0.50 $M_\odot$ we set a uniform $\log g$ prior for He-core fits to between 6.0 and 7.74 (Althaus et al. 2013; Parsons et al. 2017).

We attempt to fit both systems as He-core WDs and also both as CO-core WDs, but neither fit converges. With a binary period of $P_{\rm orb} = 3030 \pm 70$ days, WOCS 4540 is most likely the result of Case C mass transfer (See Table 1, Chen & Han 2008). Conversely, with a binary period of only $P_{\rm orb} = 120.21 \pm 0.04$ days, WOCS 5379 is most likely a Case B system. Therefore, we apply the CO-core WD $\log g$ prior to WOCS 4540 and the He-core WD $\log g$ prior to WOCS 5379. This fit does converge, and is the basis of our further analysis. (The opposite setup, applying the He-core prior to WOCS 4540 and the CO-core prior to WOCS 5379 also does not converge.)

The Markov chains were run with 500 "walkers" each for 1000 samples. We then removed the burn-in, resulting in 4×10^5 samples of the posterior.

In Figures 4 and 5 we plot 500 random draws from the posterior with each observed spectrum. The data used in the fit are shown in dark blue, with the masked sections of the spectrum (not used in the fit) shown in light blue. Adopting the 16th and 84th percentile ranges as our uncertainties, the fit results in $T_{\rm eff} = 17200^{+100}_{-80}$ K and $\log g = 7.76^{+0.03}_{-0.01}$ for WOCS 4540 and $T_{\rm eff} = 15400^{+280}_{-260}$ and $\log g = 7.45^{+0.06}_{-0.06}$ for WOCS 5379.

3.2. *Derived WD Properties*

For each sample in the posterior, we calculate the corresponding WD mass and age by interpolating across the CO-core relationships from Holberg & Bergeron

[1] https://github.com/joshspeagle/dynesty

Table 1. Properties of WOCS 4540 and WOCS 5379

Property	WOCS 4540	WOCS 5379
Previously known		
V[a]	13.857	15.372
$B-V$[a]	0.521	0.570
BSS $T_{\rm eff}$[b]	6590 ± 100 K	6400 ± 120 K
Binary period[c]	3030 ± 70 days	120.21 ± 0.04 days
Orbital eccentricity[c]	0.36 ± 0.07	0.24 ± 0.03
Fitted (16th and 84th percentile)		
WD $T_{\rm eff}$	17200^{+100}_{-80} K	15400^{+280}_{-260} K
WD $\log g$	$7.76^{+0.03}_{-0.01}$	$7.45^{+0.06}_{-0.06}$
Derived (1st and 99th percentile)		
WD mass	$0.50^{+0.05}_{-0.01}$ $M_\odot$	$0.40^{+0.04}_{-0.04}$ $M_\odot$
WD age	94^{+7}_{-3} Myr	230^{+22}_{-23} Myr

[a] from Sarajedini et al. (1999)
[b] from Gosnell et al. (2015)
[d] from Geller et al. (2009)

(2006) and Tremblay et al. (2011) for WOCS 4540 (hereafter referred to as the "Bergeron" grid[2]) and the He-core relationships from Althaus et al. (2013) for WOCS 5379. Our uncertainties are driven by errors on the fits and do not take into account possible systematic errors. As such, we adopt the 1st to 99th percentile ranges on our derived properties, resulting in masses of $M_{WD}= 0.50^{+0.05}_{-0.01}$ $M_\odot$ for WOCS 4540 and $M_{WD}= 0.40^{+0.04}_{-0.04}$ $M_\odot$ for WOCS 5379.

We note that due to the physically-driven prior in $\log g$, the allowed mass for WOCS 4540 only goes down to approximately 0.50 $M_\odot$. These results are consistent with the WD mass of WOCS 4540 being at the CO-core WD mass limit set by the Parsons et al. (2017) sample. A different assumption of the $\log g$ limit for CO-core WDs may impact the derived mass.

In Figures 6 and 7 we show contours of the posterior in $T_{\rm eff}$ and $\log g$ over a map of how these values correspond to the WD cooling age, and then the resulting histogram of ages from the posterior. The age color maps for WOCS 4540 and WOCS 5379 are created using a bilinear interpolation of the original grids of Bergeron and Althaus et al. (2013), respectively. The median age values with the 16th and 84th percentile ranges are 94^{+3}_{-2} Myr for WOCS 4540 and 230^{+12}_{-9} Myr for WOCS 5379. Adopting the 1st and 99th percentile ranges results in ages of 94^{+7}_{-3} Myr and 230^{+22}_{-23} Myr. The fitted and derived properties for the WDs are provided in Table 1.

[2] http://www.astro.umontreal.ca/~bergeron/CoolingModels

4. DISCUSSION

The presence of these systems in a well-studied cluster environment provides numerous constraints on the pre- and post-mass-transfer binary parameters. Adopting a distance to NGC 188 of 1955 pc (Section 3.1.1) and a reddening of $E(B-V) = 0.09$ (Sarajedini et al. 1999), using Modules for Experiments in Stellar Astrophysics (MESA, version 8118, Paxton et al. 2015) we establish a 6.2 Gyr age and a turnoff mass of 1.1 $M_\odot$, which is consistent with the age from Meibom et al. (2009). Between 100–300 Myr ago the main sequence turnoff was approximately 1.2 $M_\odot$. We assume that both WOCS 4540 and WOCS 5379 originally had a 1.2 $M_\odot$ primary, and hypothesize that differing progenitor binary parameters resulted in two very different BSS systems.

We first compare these systems to the Rappaport et al. (1995) theoretical relationship between final orbital period and WD mass for systems created through stable mass transfer, as shown in Figure 8. Many BSS binaries are eccentric, so we plot the WD mass against the instantaneously estimated period at periastron ($P(1-e)^{3/2}$), which is related to the separation at periastron, rather than the orbital period. The error bars for WOCS 4540 and WOCS 5379 correspond to the 1st–99th percentile mass ranges.

To illustrate the diversity of post-mass transfer binaries we also include the sample of field BSSs from

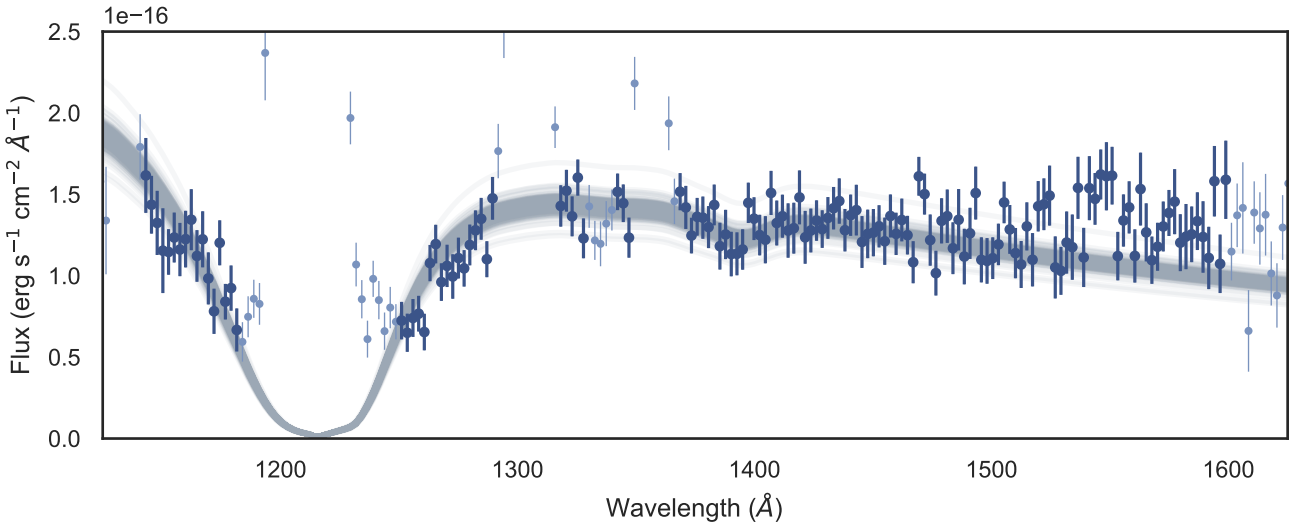

Figure 4. CO-core WD atmosphere model fits to the spectrum of WOCS 4540. The gray lines are 500 random draws from the posterior distribution. The data used in the fit are shown in darker blue, while the data masked from the fit are shown in light blue. The best fit parameters for WOCS 4540 are $T_{\rm eff} = 17200^{+100}_{-80}$ K and $\log g = 7.76^{+0.03}_{-0.01}$.

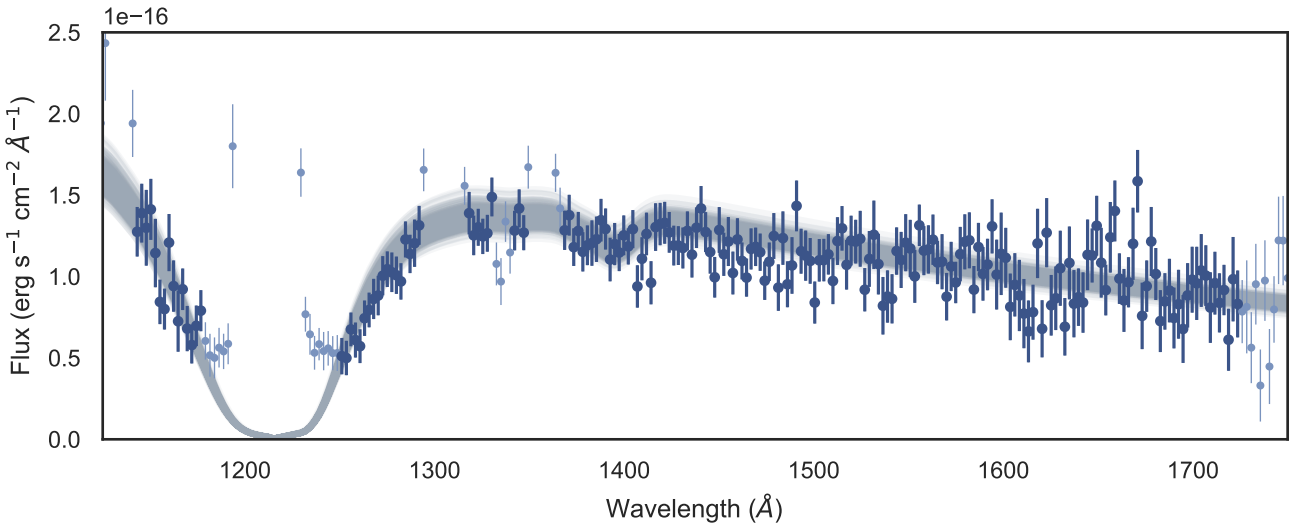

Figure 5. He-core WD atmosphere model fits to the spectrum of WOCS 5379, with the same symbols as Figure 4. The wavelength range here is different due to less contamination from the BSS companion. The best fit parameters for WOCS 5379 are $T_{\rm eff} = 15400^{+280}_{-260}$ and $\log g = 7.45^{+0.06}_{-0.06}$.

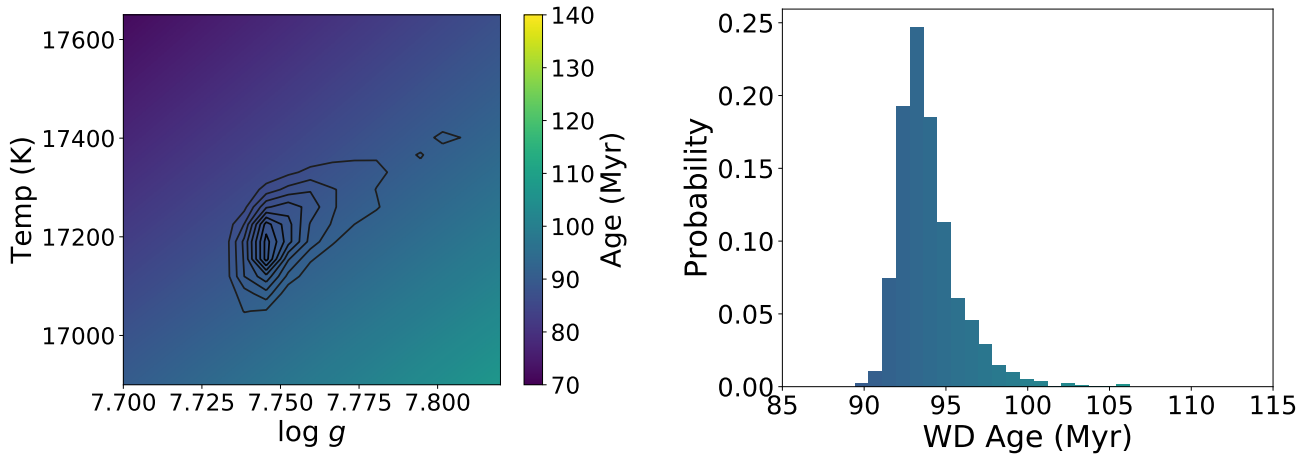

Figure 6. On the left we show contours of the posterior distribution of the `emcee` fit for WOCS 4540 in $T_{\rm eff}$ and $\log g$ on top of a color map of the corresponding WD cooling ages through this range of $T_{\rm eff}$ and $\log g$ parameter space (Holberg & Bergeron 2006; Tremblay et al. 2011). The full color map is created from a bilinear interpolation of the original Bergeron grid. The corresponding histogram of ages for WOCS 4540 is shown on the right.

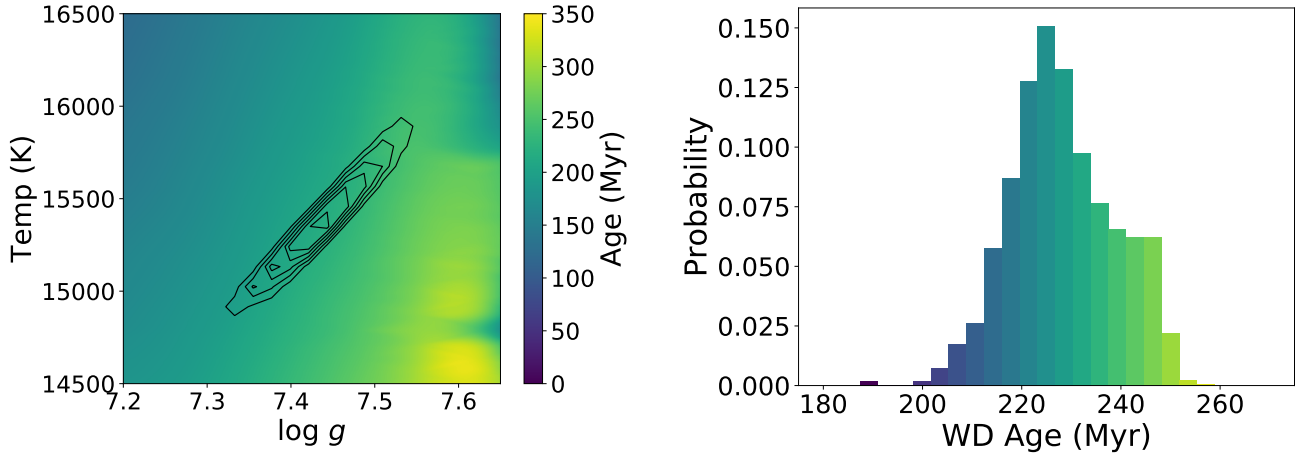

Figure 7. Same as in Figure 6, but for WOCS 5379. Here the WD cooling ages are found using Althaus et al. (2013). The structure apparent in the age color map results from the original Althaus et al. (2013) grid.

Carney et al. (2001) and self-lensing WD binary systems from Kawahara et al. (2018) and Kruse & Agol (2014). In general, many systems are consistent with the Rappaport et al. (1995) theoretical prediction for stable mass transfer but there are several systems that fall below this relationship, suggesting that post-mass transfer products can form through non-stable mass transfer processes. WOCS 4540 is entirely consistent with the Rappaport et al. (1995) relationship whereas WOCS 5379 lies just below the prediction for stable mass transfer. We return to this topic in Sections 4.3 and 4.4.

4.1. *MESA mass accretion models*

To explore the range of possible progenitor binaries we run a grid of MESA mass accretion models (Paxton et al. 2015). Comparing the HR Diagram positions of WOCS 4540 to WOCS 5379 to normal MESA evolutionary models suggests that the current observed masses of WOCS 4540 and WOCS 5379 are around 1.5–1.6 $M_{\odot}$ and 1.2–1.3 $M_{\odot}$, respectively, but we know that these stars do not have standard evolutionary histories. We instead add mass to a main sequence star such that it matches the observed characteristics of these systems at the 6.2 Gyr age of NGC 188. We are only interested

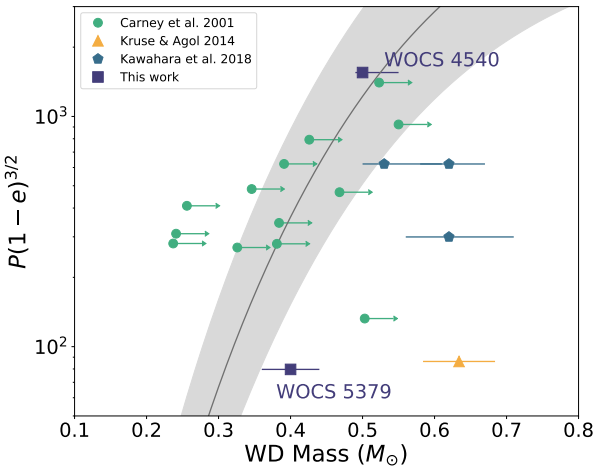

Figure 8. Post-mass transfer white dwarf binaries in the P–M_{WD} plane, modeled after Kawahara et al. (2018). In addition to the two binaries in this study, we include the sample of field BSS binaries from Carney et al. (2001) and the self-lensing WD binaries from Kruse & Agol (2014) and Kawahara et al. (2018). As many BSS binaries are eccentric, we plot WD mass against the estimated period at periastron, $P(1-e)^{3/2}$, instead of just against the orbital period. In gray we show the Rappaport et al. (1995) theoretical prediction for stable mass transfer with the upper and lower limits of the relationship (factors of 2.4) in the gray shaded region. Although some post-mass transfer systems are consistent with the prediction for stable mass transfer, including WOCS 4540, there are numerous shorter-period systems that fall below the expectations for stable mass transfer, such as WOCS 5379. The error bars for WOCS 4540 and WOCS 5279 represent the 1st–99th percentile ranges.

in the behavior of the accreting star (that will become the BSS), so we do not model the full binary evolution (which is beyond the scope of this paper). All models are single star models; we do not consider the properties of the donor or the orbital parameters of the binary system. We use the MESA test suite case `1M_pre_ms_to_wd`, but we turn off stellar rotation and do not consider rotational mixing. We assume no wind mass loss, since we are only interested in the main sequence evolution of the accretor, where the wind mass loss rates should be small.

We evolve progenitor systems ranging from 0.7–1.1 $M_\odot$ in increments of 0.1 $M_\odot$ up to an age of approximately 6 Gyr. At this point, the star accretes mass onto its surface until it reaches either 1.5 or 1.6 $M_\odot$ for WOCS 4540 or 1.2 or 1.3 $M_\odot$ for WOCS 5379. If the mass transfer is fully conservative, all of the mass leaving the donor will be accreted by the proto-BSS, and the accretion rate should equal the donor mass loss rate. Assuming the donor loses the entire envelope during the extent of the RGB or AGB phase the mass loss rate would be 10^{-8} to 10^{-6} $M_\odot$ yr^{-1}. If the mass transfer is not conservative the accretion rate will be less than the donor mass loss rate. Since we focus only on the accreting star the accretion rate is set at a constant value. We adopt a rate of 1×10^{-8} $M_\odot$ yr^{-1} which keeps the accreting stars in thermal equilibrium during accretion. We note, however, that the choice of mass transfer rate has very little impact on the final properties of the modeled BSSs. The WD cooling ages for both systems are longer than the estimated thermal timescale for both WOCS 4540 and WOCS 5379 of 70 Myr. If either system is the result of a higher mass transfer rate that drove the accretor out of thermal equilibrium, the BSS has had enough time to readjust.

Adopting 6.2 Gyr as the current age for NGC 188, we time the start of mass accretion such that it ceases at an age appropriate to the cooling age of the WD companions. We assume the composition of the accreted material matches the surface composition of the accreting star. We then allow the BSS to continue evolving to the giant branch, terminating the models when the helium core mass reaches 0.25 $M_\odot$.

The resulting evolution tracks are shown in HR diagrams in Figure 9. The bolometric luminosities for WOCS 4540 and WOCS 5379 are calculated using the relationships in Torres (2010) with temperatures from Gosnell et al. (2015), resulting in a luminosity of 10.8 ± 1.1 $L_\odot$ for WOCS 4540 and 2.7 ± 0.5 $L_\odot$ for WOCS 5379. WOCS 5379 is a photometric variable (Kafka & Honeycutt 2003), so the luminosity uncertainty includes the 0.22 mag variation in the V-band. We note that the models do not take into account any internal mixing or possible non-standard abundances as a result of the mass transfer history (see Section 4.4 for further discussion).

The symbols in Figure 9 show the location on each accretion track corresponding to an age of 6.2 Gyr, the current age of NGC 188. Comparing these symbols to the observed properties of the BSSs reveals the progenitor masses and final BSS masses most consistent with our models. WOCS 4540 appears to be closer to a 1.6 $M_\odot$ BSS than 1.5 $M_\odot$, requiring an initial progenitor of just over 1.1 $M_\odot$. (Note that stars with progenitor masses of 1.2 $M_\odot$ and higher have already evolved to the giant branch.) WOCS 5379 is close to a 1.3 $M_\odot$ BSS forming from a 0.8–0.9 $M_\odot$ progenitor.

In addition to comparing model temperatures and luminosities to these BSSs, we use the MESA colors module to compute colors and magnitudes and find models that best match the observed photometry of these systems. Here we use the spectral library of

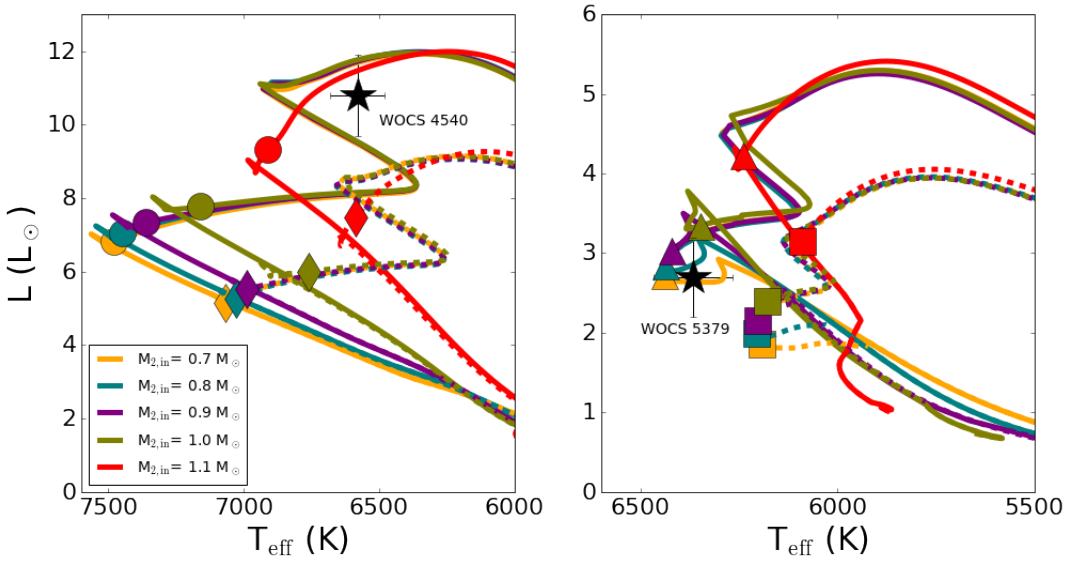

Figure 9. MESA evolutionary tracks for accreting stars with initial masses ranging from 0.7 to 1.1 $M_\odot$, as shown in the figure legend. On the left, the tracks are compared against the $T_{\rm eff}$ and luminosity of WOCS 4540, shown with a black star. Dashed lines show the accretion tracks ending with a 1.5 $M_\odot$ BSS and the solid lines show tracks ending with a 1.6 $M_\odot$ BSS, with the color indicating the original progenitor mass. The diamonds and circles show the locations on those tracks corresponding to an age of 6.2 Gyr. On the right, similar tracks are shown for WOCS 5379, with the dashed lines indicating a 1.2 $M_\odot$ BSS and the solid lines indicating a 1.3 $M_\odot$ BSS. The squares and triangles show the locations at 6.2 Gyr. These tracks show that the progenitor for WOCS 4540 must be slightly more massive than the assumed current turnoff mass of 1.1 $M_\odot$ and the resulting BSS mass is almost 1.6 $M_\odot$. WOCS 5379 has a progenitor of approximately 0.8–0.9 $M_\odot$ with a final BSS mass close to 1.3 $M_\odot$.

Lejeune et al. (1998) to compute synthetic, un-extincted B and V magnitudes for these stars. We then use a reddening of $E(B-V) = 0.09$ (Sarajedini et al. 1999) and assume a distance of 1955 pc to adjust these models to the distance and reddening of NGC 188. To find the model that best matches the photometry we explore a finer grid of MESA models with progenitors of 1.1–1.15 $M_\odot$ for WOCS 4540 and 0.8–0.9 $M_\odot$ for WOCS 5379. The models that provide the closest match to the observed BSS photometry correspond to a a 1.14 $M_\odot$ progenitor accreting mass up to 1.58 $M_\odot$ for WOCS 4540, and a 0.85 $M_\odot$ progenitor accreting mass up to 1.29 $M_\odot$ for WOCS 5379. These models are plotted on a CMD and HR Diagram of NGC 188 in Figure 10.

The final positions of the modeled stars in Figures 9 and 10 are essentially the same if we instead assume a mass transfer rate of 1×10^{-6} $M_\odot$ yr^{-1}, but the accretion paths go out of thermal equilibrium before relaxing down to a similar luminosity and temperature by 6.2 Gyr.

A sample inlist and `run_star_extras.f` routine for this model grid can be found on mesastar.org.

4.2. *Mass transfer stability*

Comparing accretion tracks to the observed properties of the BSSs constrains the parameter space of possible progenitor systems, but it does not investigate the physical response of the giant star to mass transfer, which will likely determine whether the mass transfer is expected to be stable or unstable. To understand if these accretion scenarios are possible in the context of stable Roche lobe overflow, we compute the predicted stability of the model tracks described in Section 4.1. To do this, we compare the predicted adiabatic response of a giant star to mass loss to the Roche lobe response to mass loss given various binary mass ratios and mass transfer efficiencies. For example, if the Roche lobe responds to mass loss by shrinking and the giant star responds by expanding, we would expect runaway, unstable mass transfer to occur. If, on the other hand, we expect the giant to expand while the Roche lobe also expands we could expect stable mass transfer to occur. We make these calculations at the point when mass transfer begins. We assume that mass transfer that begins as stable or unstable due to the adiabatic response of the giant star would remain so throughout the mass transfer process. Expressions for the Roche lobe and adiabatic response factors assuming a polytropic model are given in Ivanova (2015) (see also Hjellming & Webbink 1987).

The Roche lobe response factor is given by:

$$\zeta_{RL} = \frac{\partial \ln a}{\partial \ln m_d} + \frac{\partial \ln (R_{RL}/a)}{\partial \ln q} \frac{\partial \ln q}{\partial \ln m_d} \qquad (1)$$

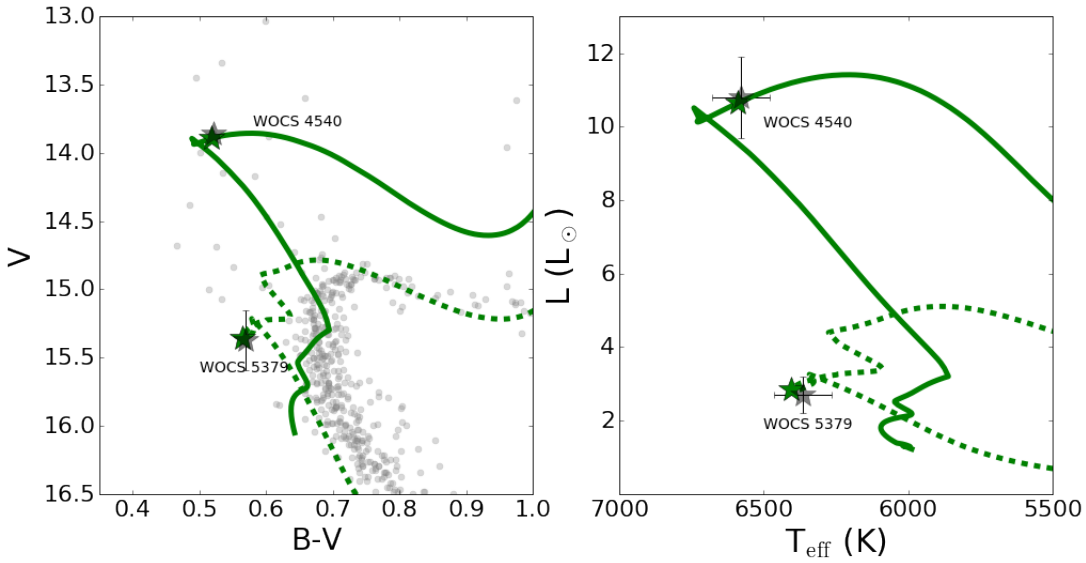

Figure 10. Left: Color-magnitude diagram showing MESA accretion evolutionary tracks for both WOCS 4540 (solid line) and WOCS 5379 (dashed line) that best match the observed photometry. The gray dots show the NGC 188 cluster members (Geller et al. 2009). The current CMD positions of both systems are shown with gray stars. The photometric errors are within the points, but WOCS 5379 is a photometric variable with ΔV= 0.22, which we show with the error bar. The modeled photometry for each track at an age of 6.2 Gyr is shown with green stars. The model that best matches WOCS 4540 is a 1.14 $M_{\odot}$ progenitor that accretes 0.44 $M_{\odot}$ to reach a final BSS mass of 1.58 $M_{\odot}$. The model that best matches WOCS 5379 is a 0.85 $M_{\odot}$ progenitor that accretes 0.44 $M_{\odot}$ to reach a BSS mass of 1.29 $M_{\odot}$. Right: The same models as on the left, but shown on an HR diagram.

where R_{RL} is the Roche lobe radius, a is the binary orbital separation, m_d is the donor mass, and q is the mass ratio of the system ($q = M_{\rm donor}/M_{\rm accretor}$). Using the Roche lobe approximation of Eggleton (1983), these partial differential equations can be approximated as:

$$\frac{\partial \ln a}{\partial \ln m_d} = \frac{2q^2 - 2 - q(1-B)}{q+1} \quad (2)$$

$$\frac{\partial \ln q}{\partial \ln m_d} = 1 + Bq \quad (3)$$

$$\frac{\partial \ln(R_{RL}/a)}{\partial \ln q} = \frac{2}{3} - \left(\frac{q^{\frac{1}{3}}}{3}\right)\frac{1.2q^{\frac{1}{3}} + 1/(1+q^{\frac{1}{3}})}{0.6q^{\frac{2}{3}} + \ln(1+q^{\frac{1}{3}})} \quad (4)$$

where B is the mass transfer efficiency (i.e. the fraction of the total mass lost by the donor that is accreted by the accretor).

The giant's adiabatic response to mass loss is given by:

$$\zeta_{ad} = \frac{2}{3}\left(\frac{m}{1-m}\right) - \frac{1}{3}\left(\frac{1-m}{1+2m}\right) - 0.03 + 0.2\left[\frac{m}{1+(1-m)^{-6}}\right] \quad (5)$$

where m is the ratio of the donor's core mass to total mass, $m = M_{\rm core}/M_{\rm donor}$.

We calculate ζ_{RL} from Equations 1–4 for every MESA model in Figure 9. Here we use two different assumptions about the donor mass as described below (taken either with or without wind mass loss) with the initial secondary mass of each model track adopted as the mass of the accreting star. The average mass transfer efficiency is calculated from:

$$B = \frac{M_{2,\rm f} - M_{2,\rm in}}{M_d - M_{\rm WD}} \quad (6)$$

where $M_{2,\rm f}$ is the final mass of the modeled BSS from our grid, $M_{2,\rm in}$ is the initial mass of the BSS progenitor, M_d is the donor mass, and $M_{\rm WD}$ is the final white dwarf mass (which we take to be either 0.40 $M_{\odot}$ or 0.50 $M_{\odot}$).

We calculate ζ_{ad} from Equation 5 using two different sets of assumptions about the donor star. In Figures 11 and 12 we compare ζ_{RL} (solid gray line) to ζ_{ad} for each MESA model in Figure 9. Where $\zeta_{RL} > \zeta_{ad}$, we expect Roche lobe overflow to lead to stable mass transfer. Where $\zeta_{RL} < \zeta_{ad}$ we expect unstable mass transfer. Therefore, any models (colored points) that fall within the gray shaded region can plausibly result from stable Roche lobe overflow. Any models above the gray shaded region we would expect to be unstable to Roche lobe overflow. In this region, unstable mass transfer would occur leading to a common envelope event which likely have very low mass transfer efficiencies (Woods & Ivanova 2011). As our best-fit models require mass transfer efficiencies over 50%, we consider unstable mass transfer to be physically unrealistic for these systems. We return to this topic in Section 4.4.

In Figure 11 we use $M_{\rm donor} = 1.2\ M_\odot$, the expected mass of an NGC 188 red giant or AGB star at an approximate age of 6.0 Gyr given no wind mass loss. Next to each point on Figure 11 we show the overall mass-transfer efficiency (B). Note that for some of our models the mass-transfer efficiency is greater than 1. This indicates a case in which the main sequence accretor must gain more material than is available from the donor in order to reach its final mass. This is nonphysical, indicating these mass-transfer models could not have occurred given our derived masses for the components of these systems.

We also consider the effect of wind mass loss on the giant branch on the stability of mass transfer, as shown in Figure 12. Here we follow the same formalism as above, but the giant star masses are determined after including a Reimers wind model (Reimers 1975) on the RGB and a Bloecker wind on the AGB (Bloecker 1995) with a scaling factor of $\eta = 0.7$. Using this wind scheme, an RGB star with an initial mass of 1.2 $M_\odot$ will have a total mass of 1.08 $M_\odot$ once the core mass reaches 0.40 $M_\odot$. An AGB star with a core mass of 0.50 $M_\odot$ will have a total mass of 0.92 $M_\odot$. The mass transfer efficiencies are recalculated considering the mass available for mass transfer after wind mass loss has occurred.

In general, reducing the giant star mass through wind mass loss moves the models toward being more stable. Wind mass loss rates on the RGB and AGB are uncertain, but we set the scaling factor at the upper end of what has been calibrated in globular clusters (McDonald & Zijlstra 2015). This provides a limit on the mass transfer scenarios that are potentially stable. We consider that a model that is unstable even with this upper-limit wind mass loss rate is unlikely to be stable when using RGB wind schemes typically found in the literature, resulting in more massive giant stars than assumed in Figure 12.

Many of the accretion scenarios modeled in Figure 9 for WOCS 4540 are not likely, either because there is not enough mass to produce the necessary BSS mass or because the mass transfer would be unstable given the secondary mass and required mass-transfer efficiency. Only models with $B < 1$ falling within the gray stability region are physically plausible (Figures 11, 12), leaving only the red and possibly green tracks as viable. However, the models that best match the temperature and luminosity of WOCS 4540 (red circles and diamonds) and the model that best matches the photometry (green star) are found to be stable regardless of the wind mass loss parameters. Although the maximal wind loss scenario that best matches the photometry requires more than 100% mass transfer efficiency, the true wind loss of the system is likely lower and would have a total mass transfer efficiency below 100%. Additionally, the total mass transfer efficiency needed is reduced if some wind mass transfer occurs in addition to stable mass transfer, which we return to in Section 4.3. We therefore conclude that WOCS 4540 can plausibly form via a standard stable mass transfer process.

On the other hand, even when using the more stable models that incorporate wind mass loss (Figure 12), the models that best match the temperature and luminosity of WOCS 5379 (blue squares and triangles) or the photometry of WOCS 5379 (green star) are still unstable. WOCS 5379 is therefore an intriguing system that challenges our assumptions about how and when mass transfer occurs.

One possible explanation for the above would be if WOCS 5379 experienced a single-binary (1+2) or binary-binary (2+2) interaction post-mass transfer that shrunk the orbit. To calculate the probability of such an interaction having occurred, we use the same assumptions for the host cluster properties of NGC 188 outlined in Section 3.2 of Leigh et al. (2011) (right-hand column). We multiply these timescales (i.e., equations A8 and A10 in Leigh et al. (2011)) by the total number of binaries in the cluster to obtain the times for a *specific* binary (i.e., WOCS 5379) to undergo a 1+2 or 2+2 interaction. This gives 1+2 and 2+2 interaction times of, respectively, approximately 35.3 Gyr and 40.3 Gyr. These timescales can be used to compute the probability of a 1+2 or 2+2 interaction having occurred post-mass transfer by taking the derived time since mass transfer ended of 250 Myr and dividing by each timescale. This gives a probability of a 1+2 or 2+2 interaction involving WOCS 5397 having occurred post-mass transfer of, respectively, approximately 0.7% and 0.6%. We conclude that the orbital properties of WOCS 5379 have a negligible probability of being affected by a dynamical interaction, meaning the observed orbit most likely reflects the orbit immediately following mass transfer.

4.3. *Formation Pathway for WOCS 4540*

The current period of WOCS 4540 of 3030 ± 70 days is traditionally thought to be too wide for Case C mass transfer (Chen & Han 2008). The eccentricity of the binary, however, brings the periastron separation of the stars close enough to be consistent with theoretical predictions for stable mass transfer, as shown in Figure 8. Although traditional binary interaction models assume that all mass transfer binaries are circularized, mass transfer from an AGB star at periastron passage can combat tidal circularization, resulting in an eccentric

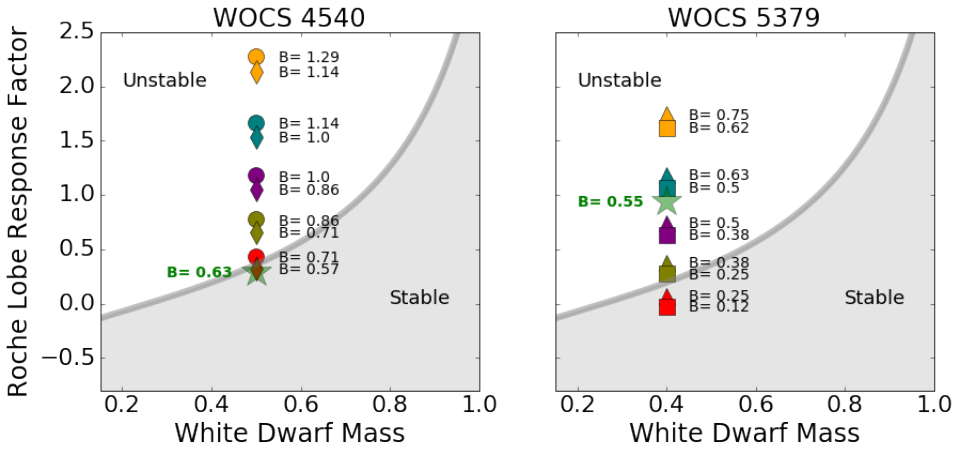

Figure 11. Stability calculations for the formation models shown in Figures 9 and 10. Models for WOCS 4540 are shown on the left, and models for WOCS 5379 are on the right. Plots compare the response of the Roche lobe to mass loss with the expected adiabatic response of the giants to mass loss as a function of the resulting white dwarf mass to the formation models (colored symbols). The shaded gray region represents mass transfer scenarios expected to be stable, where $\zeta_{RL} > \zeta_{ad}$, and the white region indicates the unstable mass transfer regime ($\zeta_{RL} < \zeta_{ad}$) where the mass-losing giant is expected to expand faster than its Roche lobe. The grey line is where $\zeta_{RL} = \zeta_{ad}$. Symbols correspond to different final blue straggler masses (1.2–1.6 $M_{\odot}$), and colors correspond to initial accretor masses (0.7–1.1 $M_{\odot}$) as in Figure 9. We also show in green stars the stability of the best-fit evolutionary tracks from Figure 10. For each model we also show the necessary mass transfer efficiency (B). Here we assume the giant donor undergoes no wind mass loss prior to the onset of Roche lobe overflow.

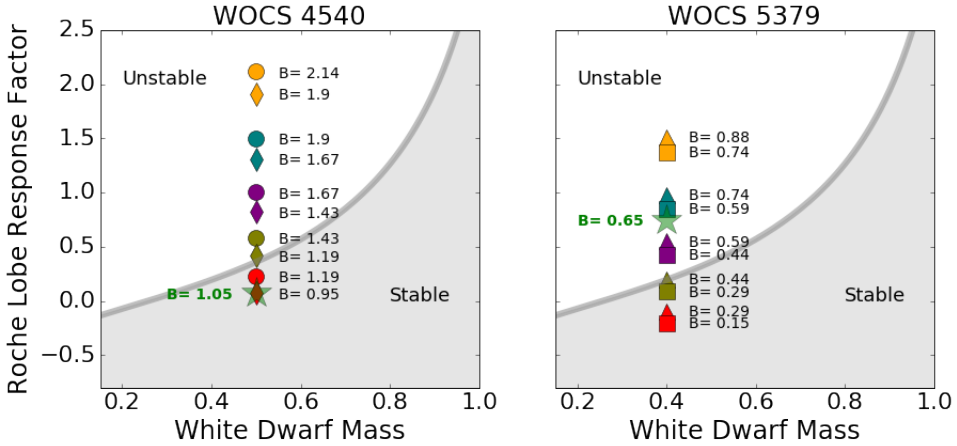

Figure 12. Stability calculations as in Figure 11, but here we determine the adiabatic response of the giant donor assuming substantial wind mass loss on the RGB, and for WOCS 4540 also on the AGB, prior to the onset of Roche lobe overflow. When accretion begins, the AGB donor for WOCS 4540 (left) has a mass of 0.92 $M_{\odot}$. The RGB donor for WOCS 5379 (right) has a mass of 1.08 $M_{\odot}$. We show the mass transfer efficiency (B) as a fraction of the mass lost during Roche lobe overflow (i.e. assuming none of the material lost earlier as a wind can be accreted by the secondary). This scenario provides an optimistic limit on the possible stability of these formation scenarios.

post-mass transfer system (Soker 2000; Bonačić Marinović et al. 2008).

Additionally, we show in Section 4.2 that the accretion evolutionary tracks that can reasonably describe the current HR Diagram and CMD location of WOCS 4540 are also consistent with a stable mass-transfer history.

We also consider the possibility that WOCS 4540 formed through an efficient wind accretion mechanism such as Wind Roche Lobe Overflow (WRLOF) (Mohamed & Podsiadlowski 2007; Abate et al. 2013). This mechanism requires the AGB wind dust formation radius to be beyond the Roche lobe radius of the system. If the wind within the dust formation radius has a

velocity less than the escape velocity of the system the Roche potential funnels the wind material toward the companion star. This can result in accretion efficiencies well beyond traditional Bondi-Hoyle-Lyttleton wind accretion (Hoyle & Lyttleton 1939; Bondi & Hoyle 1944; Mohamed & Podsiadlowski 2007). The maximum efficiency of the WRLOF is likely around 50% (Abate et al. 2013), where WOCS 4540 requires an efficiency of at least 65% to explain the luminosity and derived mass (Figure 11). It is unlikely that WRLOF is solely responsible for the mass-transfer history of WOCS 4540.

We conclude that WOCS 4540 was initially an almost equal-mass binary with a primary mass of 1.2 $M_\odot$ and a secondary mass of 1.1–1.15 $M_\odot$. The system experienced stable Roche lobe overflow mass transfer at periastron passage with a mass transfer efficiency of at least 65%. It is possible that the stable mass transfer events were augmented by WRLOF at farther separations in the eccentric orbit, or earlier in the evolution before the giant star radius reached the Roche lobe radius at periastron.

We leave the detailed modeling of the binary evolution during mass transfer to later efforts.

4.4. *Formation Pathway for WOCS 5379*

The formation of WOCS 5379 challenges our current understanding of binary mass transfer. Given the presence of a He-core WD in the system, we know the mass transfer occurred while the initial primary was on the RGB, undergoing Case B mass transfer.

The photometry of WOCS 5379 is best described by a BSS progenitor of 0.85 $M_\odot$ that accretes 0.44 $M_\odot$ to reach a final mass of 1.29 $M_\odot$ (Figure 10). The final period may be inconsistent with theoretical predictions for stable mass transfer (Figure 8) and an estimate of the adiabatic response of the 1.2 $M_\odot$ giant star to mass transfer also shows the system would be unstable (Figures 11 and 12) under a wide range of assumptions about the mass-transfer efficiency, progenitor mass, and wind mass loss prior to onset of Roche lobe overflow.

Traditionally, unstable mass transfer should cause the system to go into a common envelope phase with mass transfer efficiencies of less than 10% and with short final orbital periods on the order of days (Woods & Ivanova 2011). And yet, WOCS 5379 requires a very high mass-transfer efficiency of approximately 55% to reach both the final BSS mass necessary and the proximity to the zero-age main sequence to explain the photometry of this system. If the system has a history of unstable mass transfer, it is unclear how enough mass could have been accreted by the BSS progenitor to form WOCS 5379. Additionally, with a period of 120 days, the system is much wider than typical post-common envelope systems with periods of only a few days (Ivanova et al. 2013).

This conflict may be evidence that the application of the adiabatic approximation used in Section 4.2 is not valid in this case. Another common criteria for determining whether stable mass transfer can occur is based on the critical mass ratio ($q_c = M_{\rm donor}/M_{\rm accretor}$) needed for stable mass transfer. The traditional critical mass ratio formula used in many population synthesis codes from Hjellming & Webbink (1987) yields a critical mass ratio of just $q_c = 0.74$ compared to the $q_c = 1.4$ required for our formation model of a 1.2 $M_\odot$ red giant accreting onto a 0.85 $M_\odot$ main sequence star. Updated calculations of q_c yield somewhat higher values. For example, Woods & Ivanova (2011) suggest that including the superadiabatic response to mass loss of the surface layers of an approximately 1.0 $M_\odot$ red giant donor with a 0.4 $M_\odot$ core would yield $q_c \simeq 1.1$. Chen & Han (2008) models for BSS formation yield $q_c \simeq 1.0$ for systems similar to the model we propose for WOCS 5379. While closer, these criteria for stability still yield a q_c too low for our formation model, suggesting that more advanced mass transfer models are needed to explain the formation history of WOCS 5379.

Pavlovskii & Ivanova (2015) compare the adiabatic treatment of giant donor stars to 1D stellar models and adopt a different stability condition of whether there is overflow through the L2/L3 Lagrangian points. Importantly for this work, the L2/L3 overflow criteria can allow for stable mass transfer in binaries that fail the criteria set by the adiabatic response of the giant star. A robust comparison of WOCS 5379 to this criteria would require careful modeling of the binary evolution throughout mass transfer, which is not trivial given the non-zero eccentricity. We believe WOCS 5379 may be an important test case for the L2/L3 stability criterion in future studies.

Given the current orbital eccentricity of this system, another possibility is that mass transfer occurred in an eccentric system as we suggest also for WOCS 4540. In this case, Roche lobe overflow may only occur during periastron passage. Much is not known about mass transfer in eccentric systems, but it could increase the stability of mass transfer in this system and explain the current non-zero orbital eccentricity. WOCS 5379 and WOCS 4540 might both therefore be good test cases for new prescriptions for eccentric mass transfer (e.g., Hamers & Dosopoulou 2019).

We note also that our model assumptions of no internal mixing and no non-standard abundances could impact our interpretation of matching the accretion tracks to the observed parameters of WOCS 5379. In

particular, if the WOCS 5379 helium abundances are enhanced due to deep mixing it could impact the observed color (Sills et al. 2001) and therefore our inferred blue straggler mass. Careful consideration of abundances and internal dynamics of the mass transfer product will be important for detailed modeling efforts.

4.5. *The CMD distribution of NGC 188 BSSs*

The NGC 188 BSS population has a noticeable vertical CMD distribution (Figure 1), with what appears to be a sharp cutoff around $B - V = 0.5$ or $T_{\rm eff} \sim 7000$ K. It is now apparent that this color cutoff is a direct result of the feasibility of possible mass transfer formation pathways. The accretion tracks for WOCS 4540 in Figure 9 that result in BSSs hotter than 7000 K are not realistic, as they would require more mass to be transferred than is available in the giant star donor (Figure 11). WOCS 4540 requires a progenitor that has already evolved off of the zero-age main sequence, resulting in a cooler temperature and redder color.

We believe this limitation of possible BSS progenitors holds true for any massive BSS in NGC 188 that formed through mass transfer, creating a population of luminous BSSs that are well-separated from the zero-age main sequence and appear vertically distributed on a CMD.

5. SUMMARY

We analyze COS spectroscopy of two WD companions of BSSs WOCS 4540 and WOCS 5379 in the old open cluster NGC 188. We determine a *Gaia*-based cluster distance of 1955 pc with a Plummer sphere radius of 11 pc. We fit the $T_{\rm eff}$ and $\log g$ of these WDs, determining that WOCS 4540 has a CO-core WD with a mass of $0.50^{+0.05}_{-0.01}$ $M_\odot$ and WOCS 5379 has a He-core WD with a mass of $0.40^{+0.04}_{-0.04}$ $M_\odot$. Thus we find that both of these systems underwent mass transfer within the last 250 Myr. Given the current cluster age of 6.2 Gyr and a main sequence turnoff mass of 1.1 $M_\odot$, we conclude that both systems had giant star donors of approximately 1.2 $M_\odot$ but different initial binary parameters that led to very different BSS products.

Combining the ages of these systems with constraints derived from membership in NGC 188, we explore possible mass-transfer formation histories using a grid of MESA accretion evolutionary tracks compared to the observed physical parameters of WOCS 4540 and WOCS 5379. This comparison suggests that WOCS 4540 formed from a 1.2 $M_\odot$ and 1.15 $M_\odot$ progenitor binary that underwent mass transfer while the primary star was on the AGB. The final binary period and the accretion tracks are both consistent with stable mass transfer occurring during periastron. It is possible that stable mass transfer was enhanced by WRLOF events, especially outside of periastron passages.

WOCS 5379 likely formed from a 1.2 $M_\odot$ and 0.85 $M_\odot$ progenitor system. According to theoretical predictions of mass transfer and across a range of reasonable assumptions regarding the adiabatic response of the giant star to mass loss, WOCS 5379 does not appear to have a stable mass transfer history. WOCS 5379 requires relatively high mass transfer efficiency of at least 55% to recreate both the BSS mass and proximity to the zero-age main sequence, but unstable mass transfer is typically understood to lead to a common envelope with very low mass transfer efficiencies of less than 10% (Woods & Ivanova 2011) and a short-period orbit. Yet WOCS 5379 exists with an orbital period of 120 days. This system could be an important test case for the stability criterion used in Case B mass transfer scenarios.

WOCS 4540 and WOCS 5379 provide interesting opportunities to study mass transfer binary evolution in detail. Both have non-zero eccentricities, which is a challenge for typical binary mass transfer models that assume that systems circularize when mass transfer begins (e.g., Hurley et al. 2002). These observations can be used to constrain the parameter space for further theoretical efforts to understand mass transfer physics in detail.

We are grateful to D. Koester for sharing his grid of white dwarf atmosphere models. We thank J. J. Hermes for his insightful comments on the appropriate mass ranges for the WD fits. This paper is based on observations made with the NASA/ESA *Hubble Space Telescope*, obtained at the Space Telescope Science Institute, which is operated by the Association of Universities for Research in Astronomy, Inc., under NASA contract NAS 5-26555. These observations are associated with program #13354. E.M.L. is funded by a National Science Foundation Astronomy and Astrophysics Postdoctoral Fellowship under award No. AST-1801937.

Facilities: HST (COS)

Software: MESA (Paxton et al. 2015), numpy (van der Walt et al. 2011), astropy (Astropy Collaboration et al. 2013; Price-Whelan et al. 2018), emcee (Foreman-Mackey et al. 2013), seaborn (Waskom et al. 2014), matplotlib (Hunter 2007), scipy (Jones et al. 2001–), ipython (Prez & Granger 2007).

REFERENCES

Abate, C., Pols, O. R., Izzard, R. G., Mohamed, S. S., & de Mink, S. E. 2013, A&A, 552, A26

Althaus, L. G., Miller Bertolami, M. M., & Córsico, A. H. 2013, A&A, 557, A19

Astropy Collaboration, Robitaille, T. P., Tollerud, E. J., et al. 2013, A&A, 558, A33

Bailer-Jones, C. A. L., Rybizki, J., Fouesneau, M., Mantelet, G., & Andrae, R. 2018, AJ, 156, 58

Bloecker, T. 1995, A&A, 297, 727

Bonačić Marinović, A. A., Glebbeek, E., & Pols, O. R. 2008, A&A, 480, 797

Bondi, H., & Hoyle, F. 1944, MNRAS, 104, 273

Campello, R. J. G. B., Moulavi, D., & Sander, J. 2013, in Advances in Knowledge Discovery and Data Mining, ed. J. Pei, V. S. Tseng, L. Cao, H. Motoda, & G. Xu (Berlin, Heidelberg: Springer Berlin Heidelberg), 160–172

Cantat-Gaudin, T., Jordi, C., Vallenari, A., et al. 2018, A&A, 618, A93

Carney, B. W., Latham, D. W., Laird, J. B., Grant, C. E., & Morse, J. A. 2001, AJ, 122, 3419

Chen, X., & Han, Z. 2008, MNRAS, 387, 1416

Choi, J., Conroy, C., Ting, Y.-S., et al. 2018, ApJ, 863, 65

Eggleton, P. P. 1983, ApJ, 268, 368

Foreman-Mackey, D., Hogg, D. W., Lang, D., & Goodman, J. 2013, PASP, 125, 306

Gaia Collaboration, Prusti, T., de Bruijne, J. H. J., et al. 2016, A&A, 595, A1

Gaia Collaboration, Babusiaux, C., van Leeuwen, F., et al. 2018a, A&A, 616, A10

Gaia Collaboration, Brown, A. G. A., Vallenari, A., et al. 2018b, A&A, 616, A1

Geller, A. M., & Mathieu, R. D. 2011, Nature, 478, 356

Geller, A. M., Mathieu, R. D., Harris, H. C., & McClure, R. D. 2009, AJ, 137, 3743

Geller, A. M., Leiner, E. M., Bellini, A., et al. 2017, ApJ, 840, 66

Gosnell, N. M., Mathieu, R. D., Geller, A. M., et al. 2014, ApJL, 783, L8

—. 2015, ApJ, 814, 163

Hamers, A. S., & Dosopoulou, F. 2019, ApJ, 872, 119

Han, Z., Tout, C. A., & Eggleton, P. P. 2000, MNRAS, 319, 215

Hjellming, M. S., & Webbink, R. F. 1987, ApJ, 318, 794

Holberg, J. B., & Bergeron, P. 2006, AJ, 132, 1221

Hoyle, F., & Lyttleton, R. A. 1939, Proceedings of the Cambridge Philosophical Society, 35, 405

Hunter, J. D. 2007, Computing in Science and Engineering, 9, 90

Hurley, J. R., Tout, C. A., & Pols, O. R. 2002, MNRAS, 329, 897

Ivanova, N. 2015, Binary Evolution: Roche Lobe Overflow and Blue Stragglers, ed. H. M. J. Boffin, G. Carraro, & G. Beccari, 179

Ivanova, N., Justham, S., Chen, X., et al. 2013, Astronomy and Astrophysics Review, 21, 59

Jones, E., Oliphant, T., Peterson, P., et al. 2001–, SciPy: Open source scientific tools for Python, , , [Online; accessed ¡today¿]

Kafka, S., & Honeycutt, R. K. 2003, AJ, 126, 276

Kawahara, H., Masuda, K., MacLeod, M., et al. 2018, AJ, 155, 144

Kharchenko, N. V., Piskunov, A. E., Schilbach, E., Röser, S., & Scholz, R.-D. 2013, A&A, 558, A53

Knigge, C., Dieball, A., Maíz Apellániz, J., et al. 2008, ApJ, 683, 1006

Koester, D. 2010, Mem. Soc. Astron. Italiana, 81, 921

Kruse, E., & Agol, E. 2014, Science, 344, 275

Landsman, W., Aparicio, J., Bergeron, P., Di Stefano, R., & Stecher, T. P. 1997, ApJ, 481, L93

Landsman, W., Simon, T., & Bergeron, P. 1996, Publications of the Astronomical Society of the Pacific, 108, 250

Latham, D. W. 2007, Highlights of Astronomy, 14, 444

Leigh, N., Sills, A., & Knigge, C. 2011, MNRAS, 416, 1410

Lejeune, T., Cuisinier, F., & Buser, R. 1998, A&AS, 130, 65

Lindegren, L., Hernández, J., Bombrun, A., et al. 2018, A&A, 616, A2

Luri, X., Brown, A. G. A., Sarro, L. M., et al. 2018, A&A, 616, A9

Mathieu, R. D., & Geller, A. M. 2009, Nature, 462, 1032

—. 2015, The Blue Stragglers of the Old Open Cluster NGC 188, 29

Mathieu, R. D., & Leiner, E. M. 2019, The Impact of Binary Stars on Stellar Evolution, Cambridge Astrophysics (Cambridge University Press)

McDonald, I., & Zijlstra, A. A. 2015, MNRAS, 448, 502

Meibom, S., Grundahl, F., Clausen, J. V., et al. 2009, AJ, 137, 5086

Mohamed, S., & Podsiadlowski, P. 2007, in Astronomical Society of the Pacific Conference Series, Vol. 372, 15th European Workshop on White Dwarfs, ed. R. Napiwotzki & M. R. Burleigh, 397

Naoz, S., & Fabrycky, D. C. 2014, ApJ, 793, 137

Paczyński, B. 1971, Annual Review of Astronomy and Astrophysics, 9, 183

Parsons, S. G., Gänsicke, B. T., Marsh, T. R., et al. 2017, MNRAS, 470, 4473

Pavlovskii, K., & Ivanova, N. 2015, MNRAS, 449, 4415
Paxton, B., Marchant, P., Schwab, J., et al. 2015, ApJS, 220, 15
Perets, H. B., & Fabrycky, D. C. 2009, ApJ, 697, 1048
Piotto, G., De Angeli, F., King, I. R., et al. 2004, ApJL, 604, L109
Plummer, H. C. 1911, MNRAS, 71, 460
Prada Moroni, P. G., & Straniero, O. 2009, A&A, 507, 1575
Preston, G. W., & Sneden, C. 2000, AJ, 120, 1014
Price-Whelan, A. M., Sipőcz, B. M., Günther, H. M., et al. 2018, AJ, 156, 123
Prez, F., & Granger, B. E. 2007, Computing in Science and Engineering, 9, 21
Rappaport, S., Podsiadlowski, P., Joss, P. C., Di Stefano, R., & Han, Z. 1995, MNRAS, 273, 731
Reimers, D. 1975, Circumstellar envelopes and mass loss of red giant stars, ed. B. Baschek, W. H. Kegel, & G. Traving, 229–256
Sandage, A. R. 1953, AJ, 58, 61
Sarajedini, A., von Hippel, T., Kozhurina-Platais, V., & Demarque, P. 1999, AJ, 118, 2894
Sills, A., Faber, J. A., Lombardi, James C., J., Rasio, F. A., & Warren, A. R. 2001, ApJ, 548, 323
Sneden, C., Preston, G. W., & Cowan, J. J. 2003, ApJ, 592, 504
Soker, N. 2000, A&A, 357, 557
Subramaniam, A., Sindhu, N., Tandon, S. N., et al. 2016, ApJ, 833, L27
Torres, G. 2010, AJ, 140, 1158
Tremblay, P.-E., Bergeron, P., & Gianninas, A. 2011, ApJ, 730, 128
van der Walt, S., Colbert, S. C., & Varoquaux, G. 2011, CoRR, abs/1102.1523, arXiv:1102.1523
Waskom, M., Botvinnik, O., Hobson, P., et al. 2014, seaborn: v0.5.0 (November 2014), , , doi:10.5281/zenodo.12710
Willems, B., & Kolb, U. 2004, A&A, 419, 1057
Woods, T. E., & Ivanova, N. 2011, ApJL, 739, L48